Electrical Power and Energy Systems 58 (2014) 1–8

Contents lists available at ScienceDirect

Electrical Power and Energy Systems

journal homepage: www.elsevier.com/locate/ijepes

Power losses evaluation of a bidirectional three-port DC–DC converter for hybrid electric system

Laureano Piris-Botalla *, Germán G. Oggier, Andrés M. Airabella, Guillermo O. García

CONICET, Grupo de Electrónica Aplicada (GEA), Facultad de Ingeniería, Universidad Nacional de Río Cuarto, Ruta Nacional # 36 Km 601, X5804BYA Río Cuarto, Argentina

ARTICLE INFO

Article history:
Received 15 March 2013
Received in revised form 18 December 2013
Accepted 23 December 2013

Keywords:
Three-port DC–DC converter
Hybrid electric systems
Power losses
Soft switching

ABSTRACT

Power losses of a bidirectional three-port DC–DC converter to be used in hybrid electric systems as a function of the voltage conversion ratios and the output power are evaluated in this work. An analysis and characterization of the current on the switches into the whole converter operating range are presented. This analysis allows finding the semiconductor conduction intervals, necessary to calculate the power losses. Such losses are evaluated considering both switching and conduction semiconductor losses as well as those in the transformer. The variables used in this evaluation are voltage conversion ratios and transformer parameters like leakage inductances and turns ratios. Design considerations for the high frequency transformer that allow minimizing the total power losses are proposed. Simulation results are presented in order to validate the theoretical analysis.

1. Introduction

The use of hybrid electric systems has significantly increased due to their potential applications in hybrid electric vehicles (HEVs), renewable energy systems, microgrids, distributed generation systems, among others [1–5]. In HEV applications batteries and supercapacitors are commonly used as energy storages, due to their high energy density and their capacity to absorb or deliver peak power respectively, for example during a regenerative braking [6–8]. In these applications, the energy sources and storage devices, such as batteries and supercapacitors, may present different voltage levels respect to each other and respect to the load [9]. For this reason, it is necessary to incorporate electronic converters as interfaces between the energy sources and the load, to adapt different voltage levels and to carry out an adequate power flow control [10]. A possible solution is the use of multiport converters centralize the power flow control at only one unit in order to minimize size, cost and complexity of the system [11–13].

Different studies on multiport converters are reported in the available literature. For example, in [14,15] a bidirectional three-port DC–DC converter (TPC) is presented as a solution for hybrid fuel cell system and uninterrupted power supply applications. The power flow control consist in controlling the phase shift between the transformer voltages with fixed 50% duty-cycle.

The TPC topology can operates under soft-switching mode, which allows obtaining high efficiency [16], but this mode only can be reached within a reduced operation range, as a function of the voltage conversion ratio and the output power [11]. This is an important drawback in applications where the voltage sources change their value according to the state of charge (i.e. batteries and supercapacitors) [17].

A bidirectional converter as an interface of batteries and supercapacitors for a HEV application is proposed in [18], where the operation under soft switching mode is achieved by means of an auxiliary circuit which works twice in every switching cycle. The power losses analysis includes those produced by the auxiliary circuit. The total losses are compared with a hard switched counterpart, and it can be concluded that the converter efficiency can be increased up to 8%. In [19], an analysis of efficiency for different load conditions is carried out for the same converter topology than that presented in [18]. Soft switching mode is accomplished using a more efficient auxiliary circuit working only once at each switching instant within each switching cycle and therefore it can be concluded that this change in using the auxiliary circuit increases efficiency.

In previous papers, power losses are evaluated considering the DC voltages of the power supplies constant. For the applications considered in this paper, the voltage conversion ratios and output power could vary significantly for different operating conditions, making the evaluation of power losses a more complex problem to solve. Thus, the different operating conditions modify the conduction intervals of the power switches and the switching instants.

In this paper, an evaluation of power losses of the three-port DC–DC converter is presented. This allows obtaining design considerations for the transformer parameters like leakage inductances and turn ratios. As a result, high efficiency under different operating conditions can be obtained.

* Corresponding author. Tel./fax: +54 358 4676255.
E-mail address: lpiris@ing.unrc.edu.ar (L. Piris-Botalla).

0142-0615/$ - see front matter © 2013 Elsevier Ltd. All rights reserved.
http://dx.doi.org/10.1016/j.ijepes.2013.12.021

This work is organized as follows: Section 2 describes the TPC topology, its principle of operation and a characterization of the current waveforms. In Section 3, expressions for the TPC power losses are obtained. In Section 4, power losses are evaluated as a function of leakage inductance and voltage conversion ratios. Section 5 presents simulation results to validate the losses evaluation. Finally, conclusions are drawn in Section 6.

2. Topology description and principle of operation

The TPC topology is shown in Fig. 1. Sources V_1, V'_2 and V'_3 feed the active bridges B_1, B_2 and B_3 which convert the DC voltage into three alternating voltages, v_{T1}, v'_{T2} and v'_{T3}, respectively, to feed the high-frequency transformer, *Tr*. Each bridge can operates as rectifier or as inverter depending on the direction of the power flow. Each switch S_{xw}, shown in Fig. 1, is implemented by a power transistor, T_{xw}, and an antiparallel diode, D_{xw} [17]. The subscripts *x* and *w* represent the number of ports and switches, respectively. In this paper, V_1 represents the voltage of a battery bank, V'_2 the voltage of a supercapacitor, and V'_3 load voltage for a hybrid electric system with the particularity that V'_3 should remain constant while V_1 and V'_2 may increase or decrease depending on the operation point.

In this analysis, all the variables and parameters of ports 2 and 3, shown in Fig. 1, are referred to port 1, as follows: $L_{\ell 2} = L'_{\ell 2}/n_2^2, v_{T2} = v'_{T2}/n_2, V_2 = V'_2/n_2, i_{B2} = i'_{B2}n_2, i_{T2} = i'_{T2}n_2$ and $i_{C2} = i'_{C2}n_2$ for port 2 and $L_{\ell 3} = L'_{\ell 3}/n_3^2, v_{T3} = v'_{T3}/n_3, V_3 = V'_3/n_3, i_{B3} = i'_{B3}n_3$, $i_{T3} = i'_{T3}n_3$ and $i_{C3} = i'_{C3}n_3$ for port 3, where n_2 and n_3 are the transformer turns ratios of ports 2 and 3, respectively.

Fig. 2 shows a simplified TPC Δ-equivalent circuit, deduced in [12], which allows simplifying the power flow analysis. In this figure, the ac voltages, v_{T1}, v_{T2} and v_{T3}, represent the voltages generated by bridges, B_1, B_2 and B_3, respectively, and the inductances L_{12}, L_{13} and L_{23} can be deduced as functions of leakage inductances through a $Y-\Delta$ transformation as in [20]. The transformer magnetizing inductance is considered high enough as not to be included in the model [21].

The TPC voltage conversion ratios are defined as follows: d_{12}=$V'_2/(V_1 n_2), d_{13}$=$V'_3/(V_1 n_3)$ and the angles δ_{12} and δ_{13} are the phase shifts between v_{T1}-v_{T2} and v_{T1}-v_{T3}, respectively.

In [12] it is demonstrated that the power flow can be controlled by manipulating the phase shifts δ_{12} and δ_{13}.

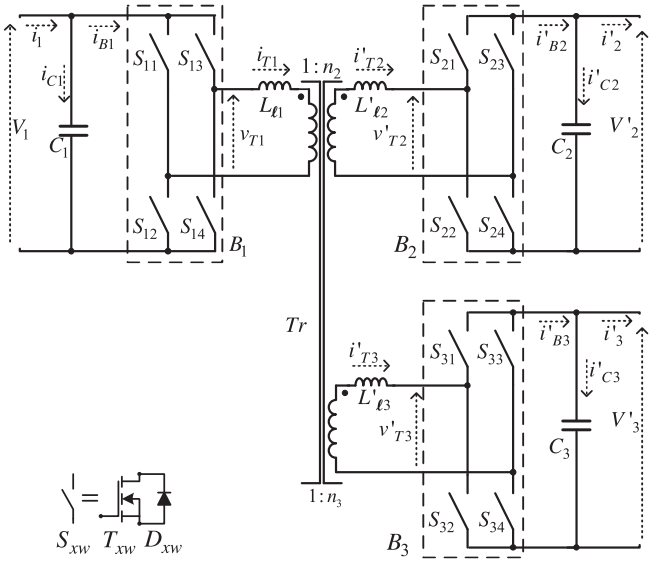

Fig. 1. Three-port bidirectional DC–DC converter topology.

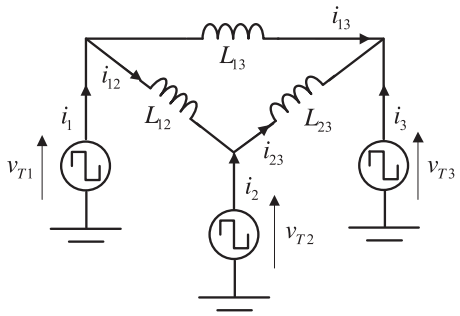

Fig. 2. TPC simplified circuit.

According to the electric equivalent circuit shown in Fig. 2, the dynamics of current along the branches can be expressed as,

$$\frac{di_{xy}(\theta)}{d\theta} = \frac{v_{Tx}(\theta) - v_{Ty}(\theta)}{\omega L_{xy}}, \tag{1}$$

where *x* and *y* represent the ports involved in the equation, $\theta = \omega t, \omega = 2\pi f_{sw}$ and f_{sw} is the switching frequency.

Solving (1), the expressions for $i_{12}(\theta), i_{23}(\theta)$ and $i_{13}(\theta)$ (see Fig. 2) can be obtained, which are also used to determine the expressions for currents at each port as follows:

$$i_1(\theta) = i_{12}(\theta) + i_{13}(\theta), \tag{2}$$
$$i_2(\theta) = i_{23}(\theta) - i_{12}(\theta), \tag{3}$$
$$i_3(\theta) = -i_{13}(\theta) - i_{23}(\theta). \tag{4}$$

Based on (2)–(4) the expressions of powers at each port of the TPC can be obtained by solving the following expression [17]

$$P_x = \frac{1}{\pi}\int_0^{\pi} v_{Tx}(\theta) i_x(\theta) d\theta. \tag{5}$$

In order to simplify notation, inductances of the Δ-equivalent circuit are normalized respect to L_{12}, as $L_2 = L_{23}/L_{12}$ and $L_3 = L_{13}/L_{12}$. Thus, the expressions for powers shown in Table 1, can be obtained as a function of V_1.

2.1. Current waveforms characterization

Fig. 3 shows the main waveforms corresponding to the equivalent circuit shown in Fig. 2: v_{T1}, v_{T2} and v_{T3}; the branch currents $i_{12}(\theta), i_{23}(\theta)$ and $i_{13}(\theta)$ and the current at each port $i_{1-a}(\theta), i_{2-a}(\theta)$ and $i_{3-b}(\theta)$ for a particular operating point given by $1 < d_{13} < d_{12}$ and $0 < \delta_{12} < \delta_{13}$. The subscripts *a* and *b* represent different cases of operating conditions which will be detailed further on.

From the same figure, it is possible to define the current stages I, II and III when $0 < \theta \leqslant \delta_{12}, \delta_{12} < \theta \leqslant \delta_{13}$ and $\delta_{13} < \theta \leqslant \pi$, respectively. The angle β_{ix-z} corresponds to $i_x(\theta)$ zero crossing of the *z* current stage. The voltage nominal values at the transformer terminal are represented in dotted lines and solid lines correspond to a particular V_1 and V'_2 DC voltage level when $d_{13} < d_{12} < 1$. This figure also shows the conducting devices at each interval.

Considering a constant DC voltage at the load port V'_3, the voltage conversion ratios, d_{12} and d_{13}, may change as functions of the state of charge of the power sources. In order to obtain a constant output power, variables δ_{12} and δ_{13} have to be adjusted when the voltage conversion ratios change. This results in different current waveforms which modify the limits of the semiconductor conduction intervals.

To determine all possible conduction intervals, it is necessary to calculate the zero crossing angles at the current ports for each active circuits. Fig. 3 and Fig. 4(a) to (d) show all the possible current

Table 1
Expressions of power at each port.

$P_1 = V_1^2(L_3\delta_{12}d_{12}\pi - L_3\delta_{12}^2 d_{12} + d_{13}\delta_{13}\pi - d_{13}\delta_{13}^2)/\omega\pi L_3$
$P_2 = V_1^2\left(d_{12}\left(2L_2\delta_{12}(\delta_{12}-\pi) + d_{12}\delta_{12}(\delta_{12}-2\delta_{13}+\pi) - d_{13}\left(\delta_{12}^2 - 4\delta_{12}\delta_{13} + 2\delta_{13}^2 + 3\delta_{12}\pi - 2\delta_{13}\pi\right)\right)\right)/2\omega\pi L_2$
$P_3 = V_1^2\left(\left(d_{12}^2 L_3\delta_{12}(\delta_{12}-2\delta_{13}+\pi) + 2d_{13}L_2\delta_{13}(-\delta_{13}+\pi) - d_{12}d_{13}L_3\left(\delta_{12}^2 + 2\delta_{13}(\delta_{13}-\pi) + \delta_{12}(-4\delta_{13}+3\pi)\right)\right)\right)/(2\omega\pi L_3 L_2)$

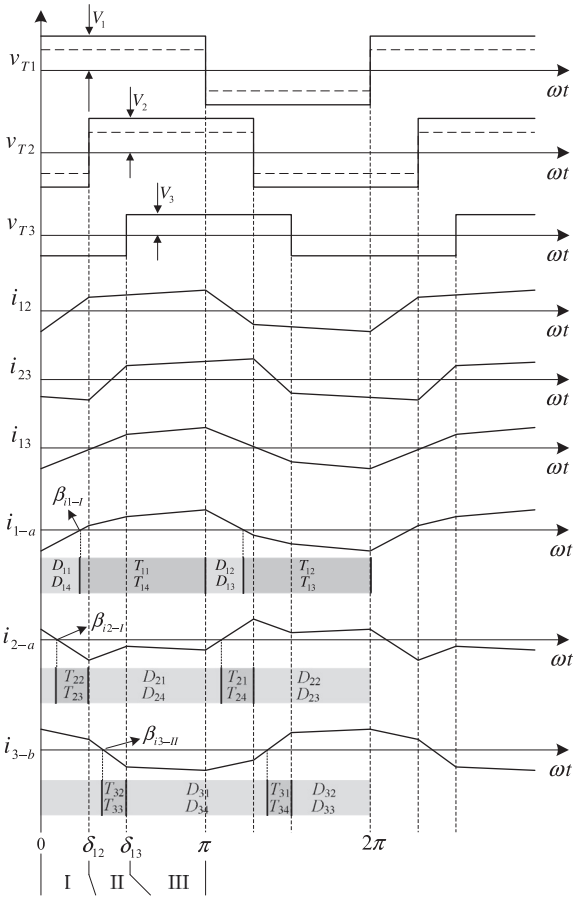

Fig. 3. Voltage and current waveforms shown in Fig. 2 for a particular operation point when $d_{13} < d_{12} < 1$ and $0 < \delta_{12} < \delta_{13}$.

waveforms at the converter ports for the particular conditions given by $0 < \delta_{12} < \delta_{13}$. The subscripts *a* to *e* represent the different cases and the conduction intervals are represented by the segments 1 to 4.

Zero-crossing angles are obtained by equating to zero each current expression, Eqs. (2)–(4), and solve them for θ, for the differents current stages I, II and III. To identify the stage at which the zero crossing occurs, the current expressions are evaluated at the beginning and at the end of each stage detecting in this way changes in the sign of the current value. Table 2 shows the expressions of the zero-crossing angles for the different current stages.

In [12], it can be observed that there is a maximum of six different cases of power flow transference between the TPC ports, depending on the phase relationship. In order to simplify the analysis and through an appropriate change of variables, it is possible to use the same inductor currents expressions for $0 < \delta_{12} < \delta_{13}$, shown in Fig. 3 and Fig. 4, to represent the other five cases. Therefore, current expressions for any voltage conversion ratios and phase shift relations of the TPC can be obtained.

3. Power losses modeling

In this section, expressions of power losses are obtained considering both conduction and switching losses and those produced in the high frequency transformer.

The semiconductor power losses are evaluated as function of the gate resistance using data available from the datasheet of the semiconductors: transconductance, internal capacitances, gate threshold voltage during switching transitions and MOSFET on-state resistances [22,23].

3.1. Power losses in semiconductor devices

The total losses produced in semiconductor devices can be divided into conduction and switching losses.

3.1.1. Conduction losses

The conduction losses are evaluated for each semiconductor device according to its current waveform and conduction interval. Table 3 shows the limits of the conduction intervals for all the possible cases aforementioned, where γ_1 represents the angle at which the device begins to conduct and γ_2 the one at which it ends.

Due to their resistive behavior, conduction power losses of the MOSFET transistors can be determined as functions of the rms current and its on-state equivalent resistance Rds_{on},

$$P_{cTx} = \left(\sqrt{\frac{1}{2\pi}\int_{\gamma_1}^{\gamma_2} i_x^2 d\theta}\right)^2 Rds_{on}. \tag{6}$$

The diode conduction losses (D_{xa} in Fig. 1) can be calculated as

$$P_{cDx} = \frac{1}{2\pi}\int_{\gamma_1}^{\gamma_2} (-V_{F(i_x)} i_x) d\theta, \tag{7}$$

where $V_{F(ix)}$ represents the diode forward voltage as a function of the current flowing through it.

Finally, the total conduction losses at port *x* can be expressed as [24]

$$P_{cx} = 4(P_{cTx} + P_{cDx}). \tag{8}$$

3.1.2. Switching losses

The expressions to evaluate the energies dissipated at the turn-off and turn-on switching transitions, as functions of the instantaneous current at the switching angles at port *x* [25], can be simplified by using linear approximations as follows:

$$E_{off(i_x)} = \frac{1}{2} V_x \, |i_x| \, (t_{ri-on} + t_{fv-on}). \tag{9}$$

$$E_{on(i_x)} = \frac{1}{2} V_x \, |i_x| \, (t_{rv-off} + t_{fi-off}), \tag{10}$$

where t_{ri-on} is the rising current time, t_{fv-on} is the falling voltage time, t_{rv-off} is the rising voltage time and t_{fi-off} is the falling current time, which are obtained as described in [26] using the information provided by the manufacturer datasheet and the driver circuit aforementioned.

Thus, power losses for turn-off can be determined as,

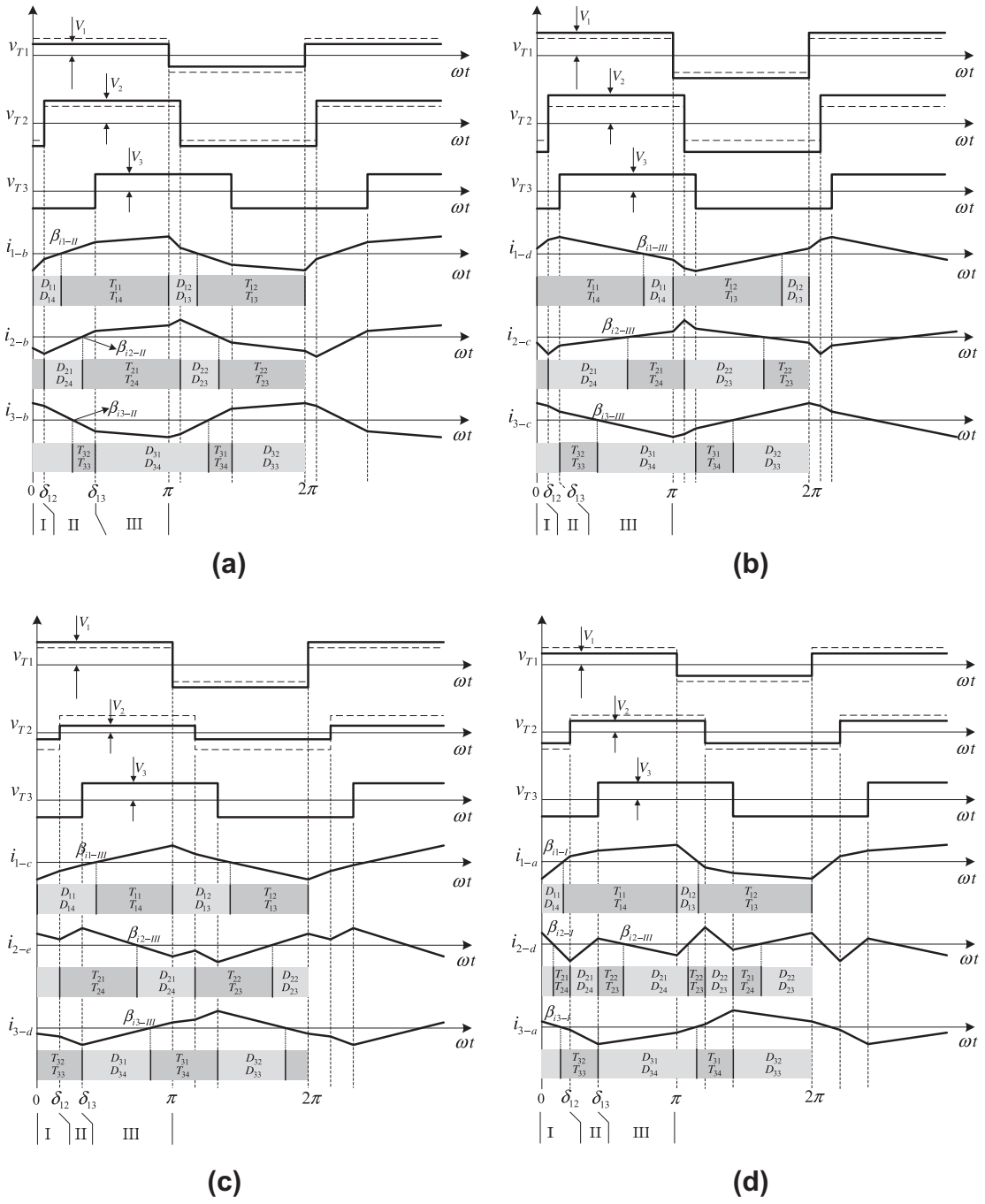

Fig. 4. Differents cases for $0 < \delta_{12} < \delta_{13}$ and voltage conversion ratios are given by (a) $d_{12} > d_{13} > 1$ (b) $d_{12} > d_{13}, d_{12} > 1$ and $d_{13} < 1$ (c) $d_{12} < d_{13} < 1$ (d) $d_{12} < d_{13}, d_{13} > 1$ and $d_{12} < 1$.

$$P_{offT_x} = E_{off(i_x)}\, f_{sw}, \tag{11}$$

whereas losses for turn-on can be determined as,

$$P_{onT_x} = E_{on(i_x)}\, f_{sw}. \tag{12}$$

As described in [27] switching losses in the power diode are due to reverse recovery current which occurs when a transistor is turned on with a non-zero current flowing through it. Therefore, turn-off power losses in the diodes can be calculated as,

$$P_{Dxoff} = V_x Q_f f_{sw} k_V, \tag{13}$$

where V_x is the voltage across the diode and k_V is a constant used to compensate for non-ideal voltage switching waveform [28]. Q_f is the effective charge producing losses. It represents part of the total charge not lost due to internal recombination [29].

Table 4 lists the turn-off and turn-on switching angles and the corresponding semiconductor devices for the particular case shown in Fig. 4(c).

3.1.3. Total losses on switches

Total losses on switches at port P_x can be determined as,

$$P_{tswx} = P_{cx} + 4(P_{swx} + P_{Dxoff}), \tag{14}$$

where P_{swx} represents P_{onT_x} or P_{offT_x}, depending on whether the switch operates under dissipative or natural switching mode during either turn-on or turn-off, respectively.

Table 2
Expressions of zero-crossing angle at each port and the corresponding waveform case.

β_{ix-z}	Expression	Case	See Fig.
β_{i1-I}	$\frac{\alpha_1 + 2L_3\phi_{12} + 2\phi_{13}}{2(1 + L_3 + d_{13} + L_3 d_{12})}$	a	3
β_{i1-II}	$\frac{\alpha_1 - 2L_3\phi_{12} + 2\phi_{13}}{2(1 + L_3 + d_{13} - L_3 d_{12})}$	b	4(a)
β_{i1-III}	$\frac{\alpha_1 - 2L_3\phi_{12} - 2\phi_{13}}{2(1 + L_3 - d_{13} - L_3 d_{12})}$	c, d	4(b and c)
β_{i2-I}	$\frac{\alpha_2 + 2\phi_{12} - 2\phi_{13} + 2L_2\phi_{12}}{2(L_2 + d_{12} - d_{13} + L_2 d_{12})}$	a, d	3, 4(d)
β_{i2-II}	$\frac{\alpha_2 - 2\phi_{12} - 2\phi_{13} - 2L_2\phi_{12}}{2(L_2 - d_{12} - d_{13} - L_2 d_{12})}$	b	4(a)
β_{i2-III}	$\frac{\alpha_2 - 2\phi_{12} + 2\phi_{13} - 2L_2\phi_{12}}{2(L_2 - d_{12} + d_{13} - L_2 d_{12})}$	c, e and d	4(b, c and e)
β_{i3-I}	$\frac{\alpha_3 - 2L_3\phi_{12} + 2L_3\phi_{13} + 2L_2\phi_{13}}{2(L_2 - L_3 d_{12} + L_3 d_{13} + L_2 d_{13})}$	a	4(d)
β_{i3-II}	$\frac{\alpha_3 + 2L_3\phi_{12} + 2L_3\phi_{13} + 2L_2\phi_{13}}{2(L_2 + L_3 d_{12} + L_3 d_{13} + L_2 d_{13})}$	b	3, 4(a)
β_{i3-III}	$\frac{\alpha_3 + 2L_3\phi_{12} - 2L_3\phi_{13} - 2L_2\phi_{13}}{2(L_2 + L_3 d_{12} - L_3 d_{13} - L_2 d_{13})}$	c and d	4(b and c)

Where $\alpha_1 = \pi + \pi L_3 - \pi d_{13} - \pi L_3 d_{12}$, $\alpha_2 = \pi L_2 - \pi d_{12} + \pi d_{13} - \pi L_2 d_{12}$, $\alpha_3 = \pi L_2 + \pi L_3 d_{12} - \pi L_3 d_{13} - \pi L_2 d_{13}$, $\phi_{12} = d_{12}\delta_{12}$ and $\phi_{13} = d_{13}\delta_{13}$.

Table 3
Device conduction intervals for all cases shown in Fig. 3 and Fig. 4.

Current	Device	γ_1	γ_2
i_{1-a}	$D_{11}D_{14}$	0	β_{i1-I}
	$T_{11}T_{14}$	β_{i1-I}	π
i_{1-b}	$D_{11}D_{14}$	0	β_{i1-II}
	$T_{11}T_{14}$	β_{i1-II}	π
i_{1-c}	$D_{11}D_{14}$	0	β_{i1-III}
	$T_{11}T_{14}$	β_{i1-III}	π
i_{1-d}	$D_{11}D_{14}$	β_{i1-III}	π
	$T_{11}T_{14}$	0	β_{i1-III}
i_{2-a}	$D_{21}D_{24}$	δ_{12}	$\pi + \beta_{i2-I}$
	$T_{21}T_{24}$	$\pi + \beta_{i2-I}$	$\pi + \delta_{12}$
i_{2-b}	$D_{21}D_{24}$	δ_{12}	β_{i2-II}
	$T_{21}T_{24}$	β_{i2-II}	$\pi + \delta_{12}$
i_{2-c}	$D_{21}D_{24}$	δ_{12}	β_{i2-III}
	$T_{21}T_{24}$	β_{i2-III}	$\pi + \delta_{12}$
i_{2-d}	$D_{21}D_{24}$	δ_{12}	δ_{13}
		β_{i2-III}	$\pi + \beta_{i2-I}$
	$T_{21}T_{24}$	δ_{13}	β_{i2-III}
		$\pi + \beta_{i2-I}$	$\pi + \delta_{12}$
i_{2-e}	$D_{21}D_{24}$	β_{i2-III}	$\pi + \delta_{12}$
	$T_{21}T_{24}$	δ_{12}	β_{i2-III}
i_{3-a}	$D_{31}D_{34}$	δ_{13}	$\pi + \beta_{i3-I}$
	$T_{31}T_{34}$	β_{i3-I}	δ_{13}
i_{3-b}	$D_{31}D_{34}$	δ_{13}	$\pi + \beta_{i3-II}$
	$T_{31}T_{34}$	$\pi + \beta_{i3-II}$	$\pi + \delta_{13}$
i_{3-c}	$D_{31}D_{34}$	β_{i3-III}	$\pi + \delta_{13}$
	$T_{31}T_{34}$	δ_{13}	β_{i3-III}
i_{3-d}	$D_{31}D_{34}$	δ_{13}	β_{i3-III}
	$T_{31}T_{34}$	β_{i3-III}	$\pi + \delta_{13}$

3.2. Transformer losses

In this paper, a toroidal core is considered for the implementation of the high frequency transformer. Transformer losses are the summation of the resistive winding losses and the magnetic core losses [17]. The resistive winding losses for each port can be calculated as

Table 4
Turn-on and turn-off switching angles and corresponding semiconductor devices for the cases shown in Fig. 4(c).

Current	Switching angle θ	P_{onTx}	P_{offTx}	P_{Dxoff}
i_{1-c}	0	–	$T_{13}T_{12}$	–
	π	–	$T_{11}T_{14}$	–
i_{2-e}	δ_{12}	$T_{21}T_{24}$	–	$D_{22}D_{23}$
	$\pi + \delta_{12}$	$T_{22}T_{23}$	–	$D_{21}D_{24}$
i_{3-d}	δ_{13}	–	$T_{32}T_{33}$	–
	$\pi + \delta_{13}$	–	$T_{31}T_{34}$	–

$$P_{cux} = I_{rmsx}^2(R_{trx}), \tag{15}$$

where I_{rmsx} is the rms value of the transformer current and R_{trx} is the effective winding resistance at the port x.

The losses associated with the magnetic core depend on the magnetic flux, the frequency, the core volume, and the voltage waveform. To simplify the calculation of these losses, the transformer can be considered to be fed by a sinusoidal voltage waveform, which allows for the following expression [17]:

$$P_{core} = V_c K_{c1} f_{sw}^{\alpha_c} B^{\beta_c} + K_{c2} f_{sw}^2 B^2, \tag{16}$$

where V_c is the core volume, B is the flux density, and K_{c1}, K_{c2}, α_c, and β_c are parameters that can be established from the core datasheet.

Total losses on the transformer can be determined as,

$$P_{tr} = P_{cu1} + P_{cu2} + P_{cu3} + P_{core}. \tag{17}$$

4. Power losses evaluation

In this section, the total power losses are evaluated for different converter operation modes. The variables used for this evaluation are voltage conversion ratios, leakage inductances and switching frequency. The parameters for the switches used in the evaluation are adopted from data sheet of SPW52N50 MOSFET and all the results shown (for space reasons) correspond to port 3 and are normalized respect to the power at that port.

4.1. Determination of leakage inductance values

In this paper, inductances $L_{\ell 1}, L'_{\ell 2}$ and $L'_{\ell 3}$ shown in Fig. 1 are needed to control the output power of the converter which have to be determined and designed carefully. These inductances correspond to the sum of the transformer leakage inductances and auxiliary inductors added in series at each port to obtain the desired inductance value. The transformer is designed in order to minimize the leakage inductance due to its leakage inductance value is difficult to control in practice.

To determine the leakage inductance values, first, those values that allow transferring the nominal power to the load are obtained. Then, an evaluation for different sets of leakage inductances is presented.

The nominal DC voltage at each port corresponds to a HEV application currently under development. These values are: $V_1 = 42\ V_{DC}$ of a battery bank, $V'_2 = 48\ V_{DC}$ of a supercapacitor and $V'_3 = 350\ V_{DC}$ with a 6 kW-load. The leakage inductances are calculated from the power expressions given in Table 1. A maximum value of $L_{12} = 1.1\ \mu$Hy, $L_{13} = 1.1\ \mu$Hy and $L_{23} = 1.1\ \mu$Hy ($L_{xy} = 1.1\ \mu$Hy) were adopted to transfer the nominal load power considering variations of 25% in the battery voltage and 50% in the supercapacitor voltage.

In order to determine the incidence of the leakage inductance on the power losses, different sets of these values were evaluated.

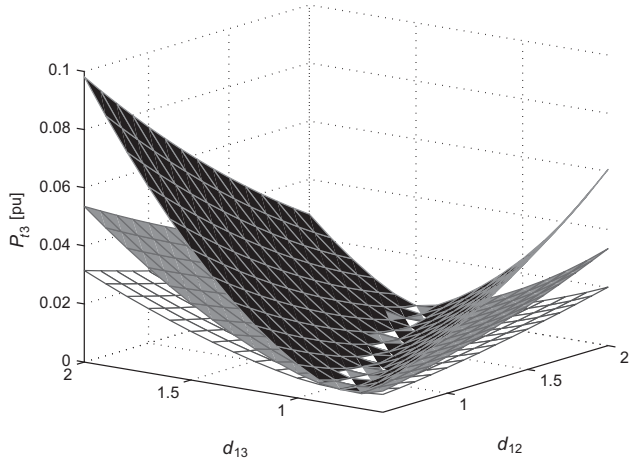

Fig. 5. Switches losses at port 3 for different leakage inductances values when the operating point of the CTP is given by $P_1 = -4$ kW, $P_2 = -200$ W, $P_3 = 4.2$ kW. The white, gray and black surfaces correspond to $L_{xy} = 1.1$ μHy, $L_{xy} = 0.75$ μHy and $L_{xy} = 0.5$ μHy, respectively.

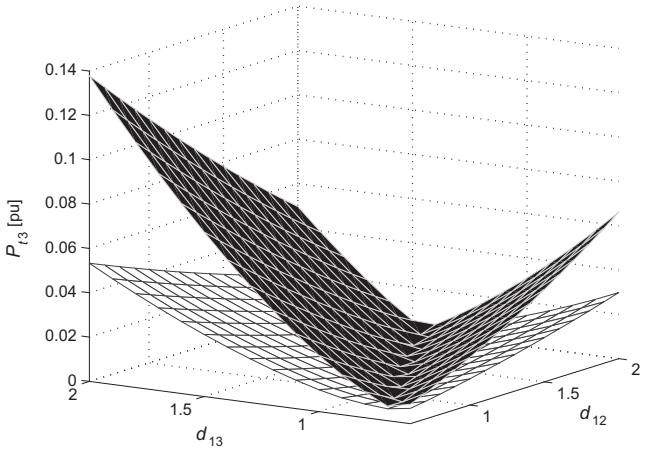

Fig. 6. P_{tsw3} with $f_{sw} = 20$ kHz (unshaded surface) and P_{tsw3} with $f_{sw} = 80$ kHz (shaded surface).

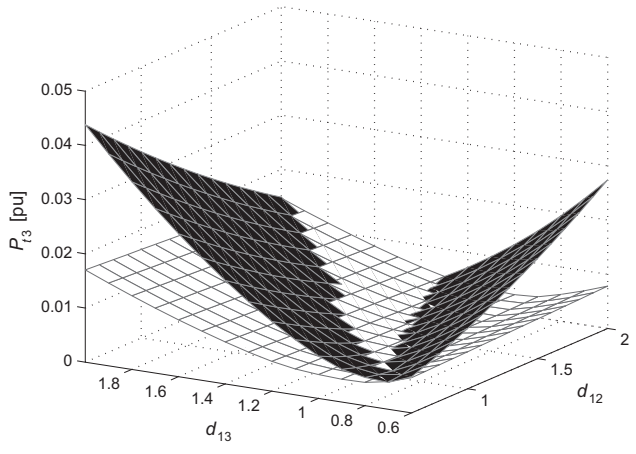

Fig. 7. Switches losses at port 3 for inductance ratios $L_{12} = L_{13} = L_{23}$ (shaded surface), $L_{12} = L_{13}$ and $L_{23} = 10L_{12}$ (unshaded surface). The operation point used in this case is: $P_1 = -3100$ kW, $P_2 = 100$ W and $P_3 = 3$ kW.

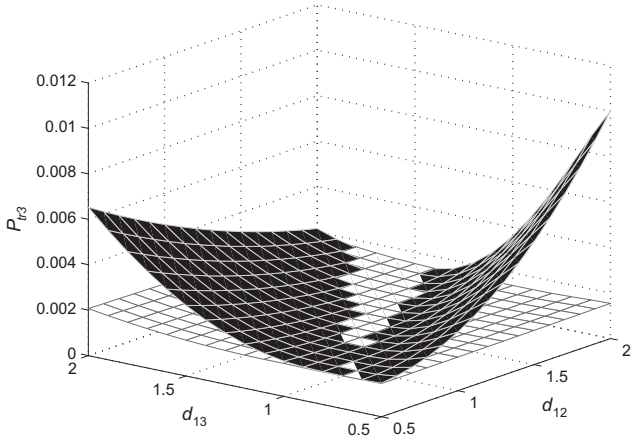

Fig. 8. Total losses in the high-frequency transformer considering conduction-winding losses at port 3 for inductance ratios $L_{12} = L_{13} = L_{23}$ (shaded surface), $L_{12} = L_{13}$ and $L_{23} = 10L_{12}$ (unshaded surface).

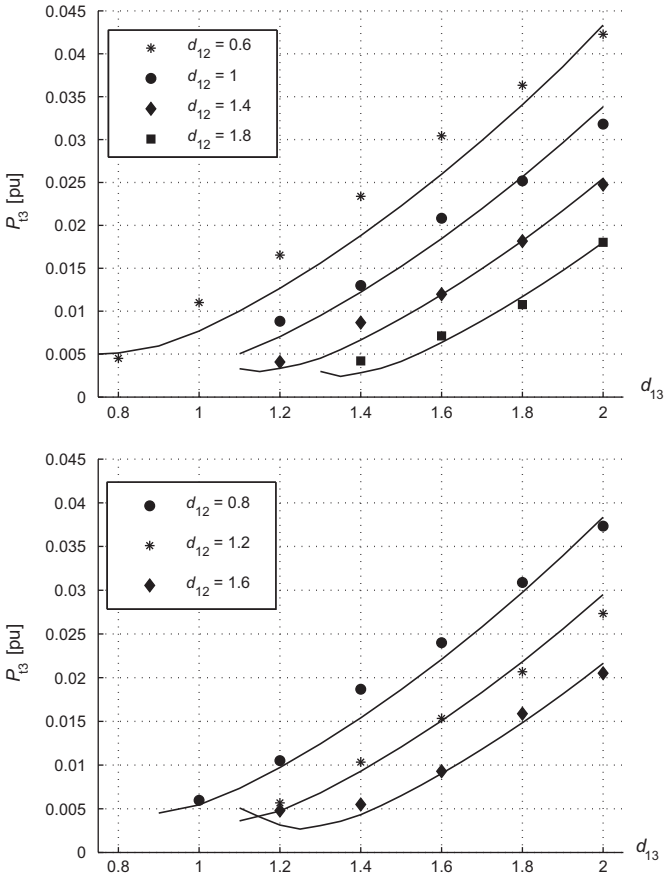

Fig. 9. Calculated and simulation results for switches losses at port 3 for leakage inductance ratios $L_{12} = L_{13} = L_{23}$.

Aiming to obtain appreciable variations in power losses, these values must be less than $L_{xy} = 1.1$ μHy. The chosen values are $L_{xy} = 0.5$ μHy,$L_{xy} = 0.75$ μHy and $L_{xy} = 1.1$ μHy. Fig. 5 shows total losses at port 3. It can be observed that for low values of leakage inductance, small changes in voltage ratios increase the switching losses. This fact can be explained due to large current at the switching instants. Results show that it is important to properly size these inductances in order to reduce the converter power losses.

What follows is an evaluation of losses at port 3 with the switching frequency as a parameter. Fig. 6 shows total losses at port 3, for the same operating point shown in Fig. 5 with a set of leakage inductances of $L_{xy} = 0.75$ μHy and a switching frequency of f_{sw}=20 kHz (unshaded surface), whereas the shaded surface shows the total losses when the switching frequency is increased to f_{sw}=80 kHz. In this figure, it can be seen that, to improve the converter power density, a 4-times increase of the switching frequency increases the power losses at port 3 up to 35%.

Besides the analysis above, which compares different sets of inductances under the relationship $L_{13} = L_{12} = L_{23}$, it is possible to find a different set of leakage inductance values that allow operating the converter with reduced power losses.

The analysis carried out in [20] shows that if L_{23} grows while L_{12} and L_{13} remain constant, the operating conditions with reduced switching losses in a wider range are achieved. However L_{23} cannot be chosen too high because the size of the inductor would be inadequate in a practical implementation which limits the maximum power to be transferred. In these evaluation, the following relationships were chosen: $L_{23} = 10L_{12}$ and $L_{13} = L_{12}$, where $L_{12} = 1.1$ μHy.

Fig. 7 represents the switches losses at port 3. In this figure, the shaded surface corresponds to the following set of inductances $L_{12} = 1.1$ μHy, $L_{13} = 1.1$ μHy and $L_{23} = 1.1$ μHy whereas the unshaded surface corresponds to $L_{12} = 1.1$ μHy, $L_{13} = 1.1$ μHy and $L_{23} = 11$ μHy. A significant reduction in power losses can be observed in the surfaces whose inductance ratio is $L_{23} = 10\ L_{12}$. This reduction is mainly due to the fact that the operation regions without energy dissipation were expanded.

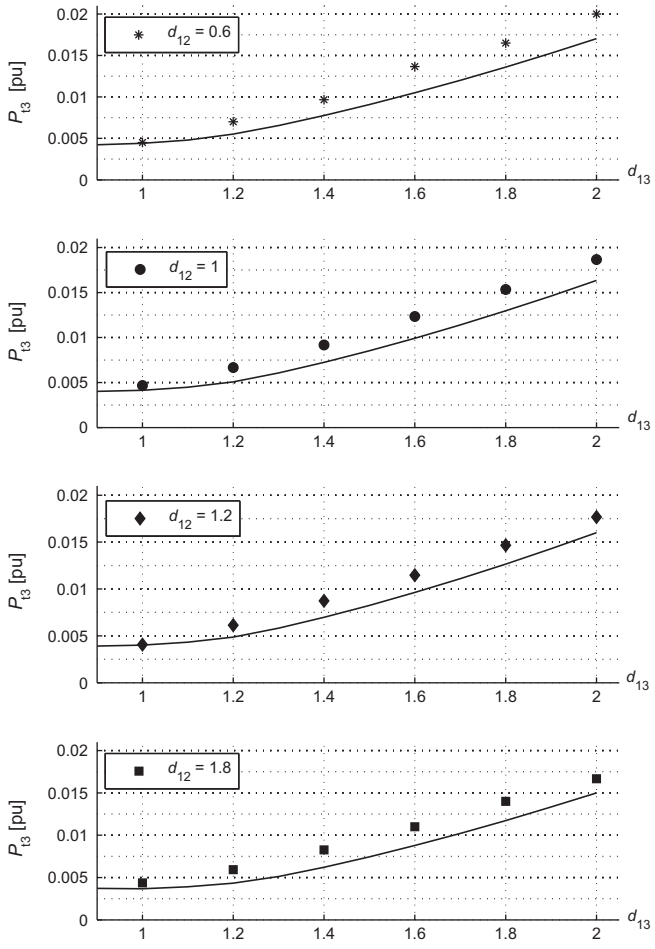

Fig. 10. Calculated and simulation results for switches losses at port 3 for leakage inductance ratios $L_{23} = 10L_{12}$ and $L_{12} = L_{13}$.

Fig. 8 shows the high frequency transformer losses considering the core losses and winding conduction losses. The core volume is $Vcore = 22.300\ mm^3$ and the winding resistance is $R_{cux} = 5$ mΩ. Also, a reduction in losses due to the rms current is produced when the inductance ratio is the same as in the previous analysis.

5. Simulation results

This section presents the simulation results to validate the power losses evaluation shown in previous section. Power loss measurements are presented for port 3, since for ports 1 and 2 similar results are obtained.

Taking into account that the mathematical model uses the switches parameters, PSpice models of the same switches are used to obtain the simulation results. The port 3 switches are SPW52N50 MOSFET. The operation point and the leakage inductance set correspond to the case shown in Fig. 7.

Fig. 9 shows the power losses obtained through simulation when d_{13} and d_{12} are the parameters. The solid line corresponds to calculations represented in shaded surface of Fig. 7 and the marks correspond to the measurements obtained from simulation. Fig. 10 shows the same results but the leakage inductance set corresponds to the case represented in the unshaded surface of Fig. 7.

In Figs. 9 and 10, the simulated power losses are compared to the calculated power losses for different operating points. Good agreement between the results obtained from the theoretical model and the simulation results are observed. A strong dependence of the efficiency on the operating point can be observed which demonstrates that the power losses increase significantly with variations in voltage conversion ratios. These figures also demonstrate that the increase in losses can be decreased by using a special set of leakage inductances.

6. Conclusion

An analysis and evaluation of the power losses on a three-port DC–DC converter with variable voltage conversion ratio and output power were carried out in this paper. The power losses considered in the analysis were semiconductor losses (conducting and switching losses) and transformer losses (winding and core losses). The preceding analysis demonstrates that the transformer leakage inductances have a significant influence on the efficiency of the converter and an adequate selection of these values is a key point in the design of the converter. The theoretical analysis, calculations, and simulation results demonstrate that a significant reduction in power losses can be achieved by using the relationship of leakage inductances of $L_{23} = 10L_{12}$.

References

[1] Barton J, Infield D. Energy storage and its use with intermittent renewable energy. IEEE Trans Energy Convers 2004;19(2):441–8.
[2] Dursun E, Kilic O. Comparative evaluation of different power management strategies of a stand-alone PV/Wind/PEMFC hybrid power system. Int J Electr Power Energy Syst 2012(34):81–9.
[3] Hajizadeh A, Golkar MA. Control of hybrid fuel cell/energy storage distributed generation system against voltage sag. Int J Electr Power Energy Syst 2010(32):488–97.
[4] Bizon N. Energy efficiency of multiport converters used in plug-in/v2g fuel cell vehicles. Appl Energy 2012(96):431–43.
[5] Tan Xingguo, Li Qingmin, Wang Hui. Advances and trends of energy storage technology in Microgrid. Int J Electr Power Energy Syst 2013(44):179–91.
[6] Burke A. Batteries and ultracapacitors for electric, hybrid, and fuel cell vehicles. Proc IEEE 2007;95(4):806–20.
[7] Mirzaei A, Jusoj A, Salam S, Adib E, Farzaehfard H. Analysis and design of a high efficiency bidirectional DC–DC converter for battery and ultracapacitor applications. Simulat Model Practice Theory 2011(19):1651–67.
[8] Fernandez LM, Garcia P, Garcia CA, Jurado F. Hybrid electric system based on fuel cell and battery and integrating a single DC/DC converter for a tramway. J Energy Convers Manage 2011(52):2183–92.

[9] Kumar Lalit, Jain Shailendra. A multiple source DC/DC converter topology. Int J Electr Power Energy Syst 2013(51):278–91.
[10] Etxeberria A, Vechiu I, Camblong H, Vinassa JM. Comparison of three topologies and controls of a hybrid energy storage system for microgrids. J Energy Convers Manage 2012(54):113–21.
[11] Tao H, Duarte J, Hendrix MAM. Three-port triple-half-bridge bidirectional converter with zero-voltage switching. IEEE Trans Power Electron 2008;23(2):782–92.
[12] Zhao C, Round S, Kolar JW. An isolated three-port bidirectional DC–DC converter with decoupled power flow management. IEEE Trans Power Electron 2008;23(5):2443–53.
[13] Vural B, Erdinc O, Uzunoglu M. Parallel combination of fc and uc for vehicular power systems using a multi-input converter-based power interface. J Energy Convers Manage 2010(51):2613–22.
[14] Michon M, Duarte J, Hendrix M, Simoes M. A three-port bi-directional converter for hybrid fuel cell systems. In: Power Electron Specialists Conference. PESC 04. IEEE 35th Annual; vol. 6. 2004, p. 4736–42.
[15] Duarte J, Hendrix M, Simoes M. Three-port bidirectional converter for hybrid fuel cell systems. IEEE Trans Power Electron 2007;22(2):480–7.
[16] Anwer Naqui, Siddiqui S Anwar, Anees S Ahmad. A lossless switching technique for smart grid applications. Int J Electr Power Energy Syst 2013;49:213–20.
[17] Oggier G, Garcia G, Oliva A. Switching control strategy to minimize dual active bridge converter losses. IEEE Trans Power Electron 2009;24(7):1826–38.
[18] Farzanehfard H, Beyragh DS, Adib E. A bidirectional soft switched ultracapacitor interface circuit for hybrid electric vehicles. J Energy Convers Manage 2008(49):3578–84.
[19] Adib E, Farzanehfard H. Soft switching bidirectional DC–DC converter for ultracapacitor-batteries interface. J Energy Convers Manage 2009(50):2879–84.
[20] Oggier G, Piris-Botalla LE, Garcia G. Soft-switching analysis for three-port bidirectional DC–DC converters. In: Industry applications conference. INDUSCON 9th IEEE/IAS. 2010, p. 1–6.
[21] Kheraluwala M, Gasgoigne R, Divan D, Bauman E. Performance characterization of a high power dual active bridge DC/DC converter. In: Industry applications society annual meeting, conference record of the IEEE, vol. 2; 1990, p. 1267–73.
[22] Wang Y, Choi S, Lee Eunchul. Efficient and ripple-mitigating DC–DC converter for residential fuell cell system. Int J Electr Power Energy Syst 2009(31):43–9.
[23] Wang Y, Cai X. DC link voltage optimized control for efficient residential fuel cell converter. Int J Electr Power Energy Syst 2010(32):1031–6.
[24] Babaei E, Mahery HM. Mathematical modeling of buck-boost DC–DC converter and investigation of converter elements on transient and steady state responses. Int J Electr Power Energy Syst 2013(44):949–63.
[25] Kovacevic G, Tenconi A, Bojoi R. Advanced DC–DC converter for power conditioning in hydrogen fuel cell systems. J Hydrogen Energy 2008(33):2315–3219.
[26] Rashid MH. Power Electronics Handbook. United States of America: Elsevier; 2007.
[27] Ulrich Nicolai Tobias Reimann JP, Lutz J. Applikationshandbuch IGBT-und MOSFET-Leistungsmodule. Nünberg, Germany: Semikron International; 1998.
[28] Schonberger J, Feix G. Modelling turn-off losses in power diodes. In: Control and modeling for power electronics. COMPEL. 11th Workshop on. 2008, p. 1–6.
[29] Mohan N, Undeland TM, Robbins WP. Power Electronics, Converters, Aplications, and Design. United States of America: Jhon Wiley & Sons, Inc.; 2003.